

Article

Thermochemistry, Structure, and Optical Properties of a New β - $\text{La}_2(\text{SO}_4)_3$ Polymorphic Modification

Sofia A. Basova¹, Maxim S. Molokeev^{2,3} , Aleksandr S. Oreshonkov^{4,5} , Maksim A. Zhernakov^{6,7} , Nikolay A. Khritokhin¹ , Aleksandr S. Aleksandrovsky^{8,9} , Alexander S. Krylov⁴ , Elena I. Sal'nikova^{1,10} , Nikita O. Azarapin^{1,11} , Natalia A. Shelpakova^{1,11}, Klaus Müller-Buschbaum^{7,12} and Yuriy G. Denisenko^{7,11,13,*} 

- ¹ Department of Inorganic and Physical Chemistry, Tyumen State University, Tyumen 625003, Russia; n.a.khritokhin@utmn.ru (N.A.K.); elenasalnikova213@gmail.com (E.I.S.); riddig@bk.ru (N.O.A.)
- ² Laboratory of Crystal Physics, Kirensky Institute of Physics, Federal Research Center KSC SB RAS, Krasnoyarsk 660036, Russia; msmolokeev@mail.ru
- ³ Laboratory of Theory and Optimization of Chemical and Technological Processes, Tyumen State University, Tyumen 625003, Russia
- ⁴ Laboratory of Molecular Spectroscopy, Kirensky Institute of Physics, Federal Research Center KSC SB RAS, Krasnoyarsk 660036, Russia; oreshonkov@iph.krasn.ru (A.S.O.); shusy@iph.krasn.ru (A.S.K.)
- ⁵ School of Engineering and Construction, Siberian Federal University, Krasnoyarsk 660041, Russia
- ⁶ A.M. Butlerov Chemistry Institute, Kazan Federal University, Kazan 420008, Russia
- ⁷ Institute of Inorganic and Analytical Chemistry, Justus-Liebig-University Giessen, 35392 Giessen, Germany
- ⁸ Laboratory of Coherent Optics, Kirensky Institute of Physics, Federal Research Center KSC SB RAS, Krasnoyarsk 660036, Russia; aleksandrovsky@kirensky.ru
- ⁹ Institute of Nanotechnology, Spectroscopy and Quantum Chemistry, Siberian Federal University, Krasnoyarsk 660041, Russia
- ¹⁰ Department of Science and Innovation, Northern Trans-Ural Agricultural University, Tyumen 625003, Russia
- ¹¹ School of Natural Sciences, Tyumen State University, Tyumen 625003, Russia
- ¹² Center for Materials Research (LaMa), Justus-Liebig-University Giessen, 35392 Giessen, Germany
- ¹³ Construction Institute, Industrial University of Tyumen, Tyumen 625000, Russia
- * Correspondence: yu.g.denisenko@gmail.com



Citation: Basova, S.A.; Molokeev, M.S.; Oreshonkov, A.S.; Zhernakov, M.A.; Khritokhin, N.A.; Aleksandrovsky, A.S.; Krylov, A.S.; Sal'nikova, E.I.; Azarapin, N.O.; Shelpakova, N.A.; et al. Thermochemistry, Structure, and Optical Properties of a New β - $\text{La}_2(\text{SO}_4)_3$ Polymorphic Modification. *Inorganics* **2023**, *11*, 434. <https://doi.org/10.3390/inorganics11110434>

Academic Editor: Hans-Conrad zur Loye

Received: 9 October 2023

Revised: 3 November 2023

Accepted: 7 November 2023

Published: 9 November 2023



Copyright: © 2023 by the authors. Licensee MDPI, Basel, Switzerland. This article is an open access article distributed under the terms and conditions of the Creative Commons Attribution (CC BY) license (<https://creativecommons.org/licenses/by/4.0/>).

Abstract: A new polymorphic modification of lanthanum sulfate was obtained by thermal dehydration of the respective nonahydrate. According to powder X-ray diffraction, it was established that β - $\text{La}_2(\text{SO}_4)_3$ crystallized in the C2/c space group of the monoclinic system with the $\text{KTh}_2(\text{PO}_4)_3$ structure type ($a = 17.6923(9)$, $b = 6.9102(4)$, $c = 8.3990(5)$ Å, $\beta = 100.321(3)^\circ$, and $V = 1010.22(9)$ Å³). Temperature dependency studies of the unit cell parameters indicated almost zero expansion along the a direction in the temperature range of 300–450 K. Presumably, this occurred due to stretching of the $[\text{LaO}_9]_n$ chains along the c direction, which occurred without a significant alteration in the layer thickness over the a direction. A systematic study of the formation and destruction processes of the lanthanum sulfates under heating was carried out. In particular, the decisive impact of the chemical composition and formation energy of compounds on the thermodynamic and kinetic parameters of the processes was established. DFT calculations showed β - $\text{La}_2(\text{SO}_4)_3$ to be a dielectric material with a bandgap of more than 6.4 eV. The processing of β - $\text{La}_2(\text{SO}_4)_3$ with the Kubelka–Munk function exhibited low values below 6.4 eV, which indicated a fundamental absorption edge above this energy that was consistent with LDA calculations. The Raman and infrared measurements of β - $\text{La}_2(\text{SO}_4)_3$ were in accordance with the calculated spectra, indicating that the obtained crystal parameters represented a reliable structure.

Keywords: rare earths; lanthanum; sulfate; crystal chemistry; thermodynamics; chemical kinetics; dielectrics

1. Introduction

Rare earth elements (REEs) are prominent in modern science as they are essential components in the transition toward green technologies. In particular, this review revealed recent articles describing their extraction processes from various sources [1–7], as REE forms numerous compounds with inorganic and organic ligands. Indeed, a wide range of such compounds was examined, for instance halides, nitrates, sulfates, carbonates, phosphates, oxalates, hydroxides, and oxides, as well as double salts [8–13].

The sulfates of rare earths are perhaps the most frequently studied group of inorganic complex compounds due to their wide range of applications [14–21]. The thermodynamic properties of these compounds occupy an important position in various hydrometallurgical processes for REE production [22]. Since the discovery of rare earths, sulfates have also been critical in the separation processes [23–30]. In addition, applications of $\text{Ln}_2(\text{SO}_4)_3$ (Ln^{3+} –REE) was proposed as a new feasible system for thermal energy storage [31].

The majority of known studies focus on hydrates of lanthanide sulfates. Usually, the hydrated species under investigation are $\text{Ln}_2(\text{SO}_4)_3 \cdot 8\text{H}_2\text{O}$ octahydrates, which have been determined throughout the whole lanthanide series, including yttrium. Sulfates with different water contents have been mainly found for larger Ln^{3+} ions, namely La–Nd. In particular, $\text{Ln}_2(\text{SO}_4)_3 \cdot 9\text{H}_2\text{O}$ nonahydrates are known for $\text{Ln} = \text{La}^{3+}, \text{Ce}^{3+}$. Pentahydrates $\text{Ln}_2(\text{SO}_4)_3 \cdot 5\text{H}_2\text{O}$ have been established for $\text{Ln} = \text{Ce}^{3+}, \text{Nd}^{3+}$, while $\text{Ln}_2(\text{SO}_4)_3 \cdot 4\text{H}_2\text{O}$ tetrahydrates have been detected for $\text{Ln} = \text{La}^{3+}, \text{Ce}^{3+}, \text{Nd}^{3+}, \text{Tb}^{3+}, \text{Er}^{3+}, \text{Lu}^{3+}$, [32], and Eu^{3+} [33] ions. Up until now, only three water molecules have been identified in the $\text{Lu}_2(\text{SO}_4)_3 \cdot 3\text{H}_2\text{O}$ compound [32]. In addition, the presence of lanthanum sulfate monohydrate $\text{La}_2(\text{SO}_4)_3 \cdot \text{H}_2\text{O}$ was recently reported [33].

Thus, crystallohydrates can be found for almost all known lanthanum sulfates. However, our review did not revealed adequate clarity in the available literature regarding the related anhydrous phases for both rare earth sulfates in general, and for lanthanum sulfate in particular. To this end, the corresponding monoclinic anhydrous sulfates $\text{Ln}_2(\text{SO}_4)_3$ ($\text{Ln} = \text{Pr}$ [34], Nd [35], and Eu [36]) have been comprehensively characterized in the case of light REEs. It can be assumed that the structure of lanthanum sulfate is similar to this group of compounds. However, lanthanum often exhibits properties distinct from those of the whole series of lanthanides, because the La–Ce interface is a region of structural instability [37,38]. Hence, new structural types are expected to emerge.

M. S. Wickleder discovered the formation of anhydrous lanthanum sulfate during the study of thermal decomposition processes for lanthanum amidosulfates [39]. Although a detailed structural study of this phase has not been carried out, the determined unit cell parameters allow us to presume that during the decomposition of amidosulfates, anhydrous lanthanum sulfate is formed, adopting the $\text{Nd}_2(\text{SO}_4)_3$ structural type [35]. In the present work, we studied a new polymorphic modification of lanthanum sulfate, which was assigned the β designation.

2. Results and Discussion

2.1. Thermochemistry of Formation and Thermal Stability

The DTA/TG method was used to investigate the formation process of anhydrous lanthanum sulfate through the dehydration of $\text{La}_2(\text{SO}_4)_3 \cdot 9\text{H}_2\text{O}$ (Figure 1). All of the thermal effects concerning the weight loss were consistent with the corresponding chemical processes (Table 1). We established four stages (signals A–D) that describe the nonahydrate dehydration process. In particular, in the first stage (signal A) within the temperature range of 75–160 °C, five water molecules were removed simultaneously, leading to the formation of the $\text{La}_2(\text{SO}_4)_3 \cdot 4\text{H}_2\text{O}$ compound. In the second stage (signal B), the tetrahydrate decomposed with the loss of two more water molecules. As the thermal effects of these processes overlapped, it was complicated to determine a stability temperature range for the corresponding tetrahydrate. Nevertheless, mathematical processing resulted in an approximate value of 140–205 °C. In the third stage (signal C), within a temperature range of 205–240 °C, the $\text{La}_2(\text{SO}_4)_3 \cdot 2\text{H}_2\text{O}$ dihydrate decomposed to form the respective

monohydrate. Afterward, the $\text{La}_2(\text{SO}_4)_3 \cdot \text{H}_2\text{O}$ compound lost a water molecule (fourth signal), resulting in the formation of anhydrous lanthanum sulfate (signal D).

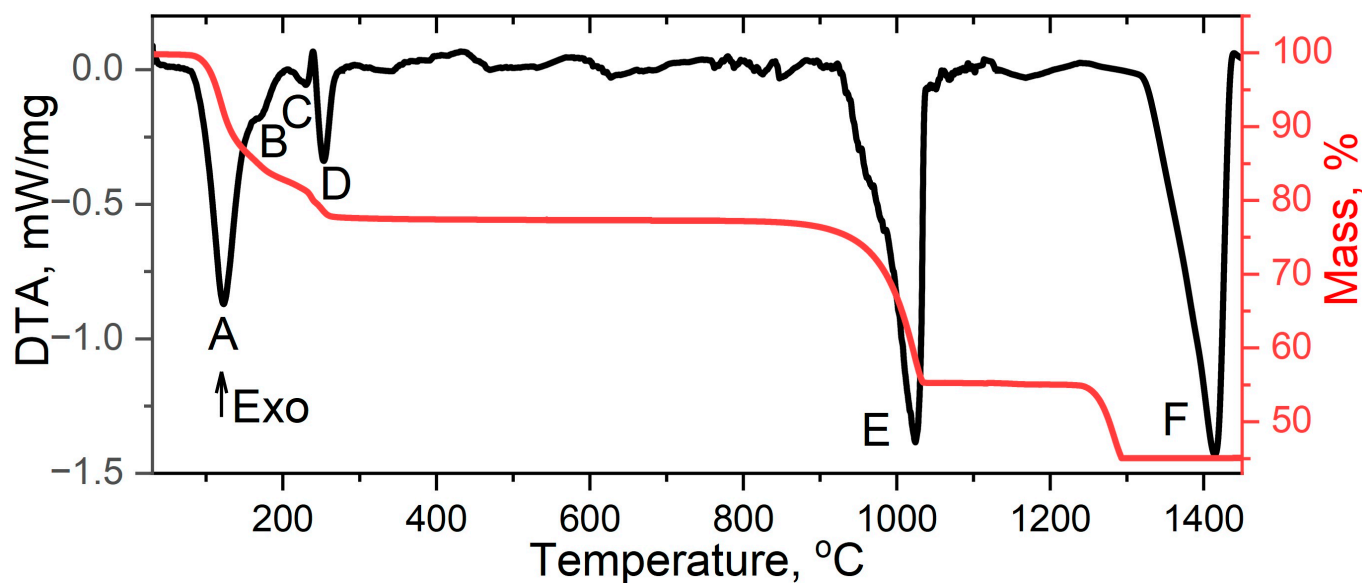


Figure 1. DTA/TG curves of $\text{La}_2(\text{SO}_4)_3 \cdot 9\text{H}_2\text{O}$ thermal decomposition.

Table 1. Thermal effects recorded during the decomposition of $\text{La}_2(\text{SO}_4)_3 \cdot 9\text{H}_2\text{O}$.

Signal	Chemical Process	$\Delta m_{\text{exp.}}, \%$	$\Delta m_{\text{theor.}}, \%$	$\Delta H, \text{kJ/mol}$
A	$\text{La}_2(\text{SO}_4)_3 \cdot 9\text{H}_2\text{O} \rightarrow \text{La}_2(\text{SO}_4)_3 \cdot 4\text{H}_2\text{O} + 5\text{H}_2\text{O}$	−12.42	−12.37	345.87
B	$\text{La}_2(\text{SO}_4)_3 \cdot 4\text{H}_2\text{O} \rightarrow \text{La}_2(\text{SO}_4)_3 \cdot 2\text{H}_2\text{O} + 2\text{H}_2\text{O}$	−17.34	−17.32	101.45
C	$\text{La}_2(\text{SO}_4)_3 \cdot 2\text{H}_2\text{O} \rightarrow \text{La}_2(\text{SO}_4)_3 \cdot \text{H}_2\text{O} + \text{H}_2\text{O}$	−19.81	−19.79	12.52
D	$\text{La}_2(\text{SO}_4)_3 \cdot \text{H}_2\text{O} \rightarrow \beta\text{-La}_2(\text{SO}_4)_3 + \text{H}_2\text{O}$	−22.34	−22.41	56.40
E	$\beta\text{-La}_2(\text{SO}_4)_3 \rightarrow \text{La}_2\text{O}_2\text{SO}_4 + 2\text{SO}_2 + \text{O}_2$	−44.22	−44.25	610.22
F	$\text{La}_2\text{O}_2\text{SO}_4 \rightarrow \text{La}_2\text{O}_3 + \text{SO}_2 + \frac{1}{2}\text{O}_2$	−55.20	−55.25	721.28

The enthalpy values of the dehydration processes tended to diminish with the simplification of the chemical composition. However, the removal of the last water molecule was associated with a much larger energy expenditure than the removal of one water molecule from the corresponding $\text{La}_2(\text{SO}_4)_3 \cdot 2\text{H}_2\text{O}$ dihydrate, which indicated the extremely low stability of the latter.

Table 2 summarizes the kinetics characteristics for all of the chemical processes detected using differential thermal analysis, which were then evaluated using the Kissinger and Ozawa–Doyle equations. Figure S1 shows the dependence of the extreme thermal effects on the heating rate. The curves demonstrated a linear shift in the maxima of thermal effects when the heating rate changed. This allowed the data to be processed reliably using linear kinetic equations.

Dehydration of $\text{La}_2(\text{SO}_4)_3 \cdot 9\text{H}_2\text{O}$, like other comparable crystalline hydrates, began at a relatively low temperature, although in this case, the crystallization water was only partially lost. Despite having the highest lability (kinetic instability) among all of the similar crystalline hydrates, the dehydration thermodynamic stability of $\text{La}_2(\text{SO}_4)_3 \cdot 9\text{H}_2\text{O}$ was the highest. Indeed, the activation energy did not exceed 65 kJ/mol for stage A, 71 kJ/mol for complete dehydration of the $\text{Eu}_2(\text{SO}_4)_3 \cdot 8\text{H}_2\text{O}$ compound [16], and 77 kJ/mol for the $\text{Pr}_2(\text{SO}_4)_3 \cdot 8\text{H}_2\text{O}$ compound [34]. Moreover, stage A enthalpy was almost 346 kJ/mol, while for the complete dehydration process of the $\text{Pr}_2(\text{SO}_4)_3 \cdot 8\text{H}_2\text{O}$ and $\text{Eu}_2(\text{SO}_4)_3 \cdot 8\text{H}_2\text{O}$ substances, this parameter was only 109 kJ/mol.

Table 2. Kinetic parameters of the decomposition of lanthanum sulfates.

Chemical Process	Kinetic Parameters		
	Kissinger Equation		Ozawa-Doyle Equation
	E_a , kJ/mol	A	E_a , kJ/mol
$\text{La}_2(\text{SO}_4)_3 \cdot 9\text{H}_2\text{O} \rightarrow \text{La}_2(\text{SO}_4)_3 \cdot 4\text{H}_2\text{O} + 5\text{H}_2\text{O}$	65	1.07×10^8	67
$\text{La}_2(\text{SO}_4)_3 \cdot 4\text{H}_2\text{O} \rightarrow \text{La}_2(\text{SO}_4)_3 \cdot 2\text{H}_2\text{O} + 2\text{H}_2\text{O}$	343	2.01×10^{40}	315
$\text{La}_2(\text{SO}_4)_3 \cdot 2\text{H}_2\text{O} \rightarrow \text{La}_2(\text{SO}_4)_3 \cdot \text{H}_2\text{O} + \text{H}_2\text{O}$	232	6.39×10^{23}	223
$\text{La}_2(\text{SO}_4)_3 \cdot \text{H}_2\text{O} \rightarrow \beta\text{-La}_2(\text{SO}_4)_3 + \text{H}_2\text{O}$	147	1.15×10^{14}	147
$\beta\text{-La}_2(\text{SO}_4)_3 \rightarrow \text{La}_2\text{O}_2\text{SO}_4 + 2\text{SO}_2 + \text{O}_2$	320	1.79×10^{11}	323
$\text{La}_2\text{O}_2\text{SO}_4 \rightarrow \text{La}_2\text{O}_3 + \text{SO}_2 + \frac{1}{2}\text{O}_2$	422	1.26×10^{12}	424

Pre-exponential factor A for the described processes was two orders of magnitude larger in the case of the lanthanum compound ($A = 10^8$) than the value for the compounds of Pr^{3+} ($A = 6 \cdot 10^6$) [34] and Eu^{3+} ($A = 10^6$) [16]. This phenomenon corresponded to larger values of activation entropy and steric factors during the dehydration process of $\text{La}_2(\text{SO}_4)_3 \cdot 9\text{H}_2\text{O}$ compared with the $\text{Pr}_2(\text{SO}_4)_3 \cdot 8\text{H}_2\text{O}$ and $\text{Eu}_2(\text{SO}_4)_3 \cdot 8\text{H}_2\text{O}$ compounds. This phenomenon was consistent with the lower anisotropy and greater symmetry of the lanthanum compound (hexagonal lattice) compared with the praseodymium and europium compounds (monoclinic lattice).

In terms of thermodynamics and kinetics, the subsequent dehydration processes (signals B, C, and D) were characterized by a significantly lower stability of intermediate crystalline hydrates and their increased inertness, respectively. The decrease in anisotropy (higher values for the pre-exponential factor of the processes) indicated a more symmetrical arrangement of the remaining water molecules in the coordination sphere of lanthanum in the decomposition products.

The anhydrous lanthanum sulfate that emerged after complete dehydration was stable up to 860 °C, with an outstanding thermal stability similar to other anhydrous light REE sulfates [34–36]. In the temperature range of 860–1050 °C, the first stage of $\beta\text{-La}_2(\text{SO}_4)_3$ decomposition (signal E) was detected, which corresponded to the formation of the lanthanum oxysulfate $\text{La}_2\text{O}_2\text{SO}_4$. The latter then decomposed in the temperature range of 1300–1440 °C into the lanthanum oxide La_2O_3 (signal F). The values of enthalpies of the decomposition processes (Table 1) indicated the high thermodynamic stability of the $\beta\text{-La}_2(\text{SO}_4)_3$ and $\text{La}_2\text{O}_2\text{SO}_4$ sulfates.

Figure 2 demonstrates the dependencies of both parameter types of the $\text{Ln}_2(\text{SO}_4)_3$ and $\text{Ln}_2\text{O}_2\text{SO}_4$ ($\text{Ln} = \text{La}, \text{Pr}$ [34], Eu [16]) decomposition reactions on the ionic radius of the Ln^{3+} ion. It should be noted that the crystal structure of $\beta\text{-La}_2(\text{SO}_4)_3$ differed from the isostructural sulfates of praseodymium and europium. Their decomposition parameters tended to decrease as the atomic number increased (Figure 2a), while the difference in parameters was significantly greater in the La–Pr pair than in the Pr–Eu pair, which, in general correlated with the difference in the crystal structure. The decomposition parameters of isostructural oxysulfates $\text{Ln}_2\text{O}_2\text{SO}_4$ ($\text{Ln} = \text{La}, \text{Pr}, \text{and Eu}$) also showed a tendency to decrease among the lanthanide series (Figure 2b), but with a clear breakpoint that occurs at the praseodymium. Presumably, this fact is related to the formation energy of the corresponding oxide. In particular, Pr_6O_{11} oxide has the lowest enthalpy of formation and the highest stability. This fact requires a reduction in the energy consumption of the system, according to the considerations of both thermodynamics and kinetics.

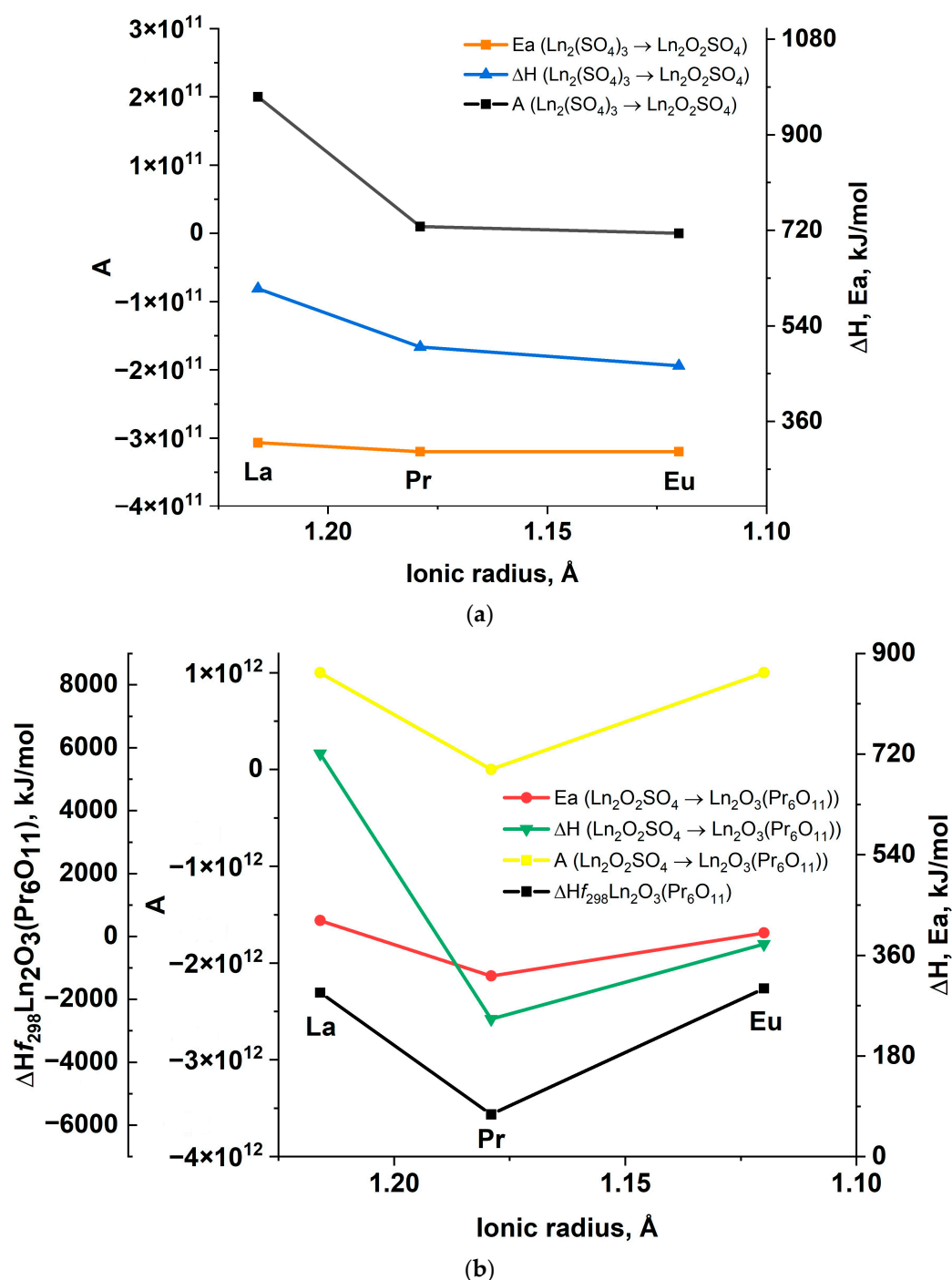


Figure 2. Character of variations in thermodynamic and kinetics parameters of processes Ln₂(SO₄)₃ → Ln₂O₂SO₄ (a) and Ln₂O₂SO₄ → Ln₂O₃(Pr₆O₁₁) (b) depending on the radius of the Ln³⁺ ion.

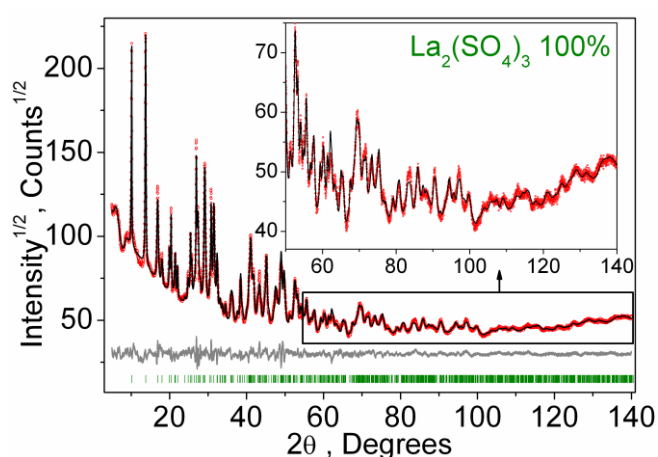
In the decomposition processes of β-La₂(SO₄)₃ and La₂O₂SO₄ (signals E and F), their increased inertness (higher activation energies of the process) compared with the same compounds of praseodymium and europium could be noticed. Indeed, for the DTA curves, the peaks were broader in the case of the lanthanum compounds. The β-La₂(SO₄)₃ and La₂O₂SO₄ thermal and thermodynamic stability were the highest as well, as the enthalpies of stages E and F were 610 kJ/mol and 721 kJ/mol, respectively. The praseodymium compound was the least inert among the Ln₂O₂SO₄ series, which was possibly related to a predisposition to form Pr₆O₁₁ oxide with cubic symmetry. In addition, decomposition temperatures also consistently diminished in the series of La–Pr–Eu compounds.

2.2. Crystal Structure

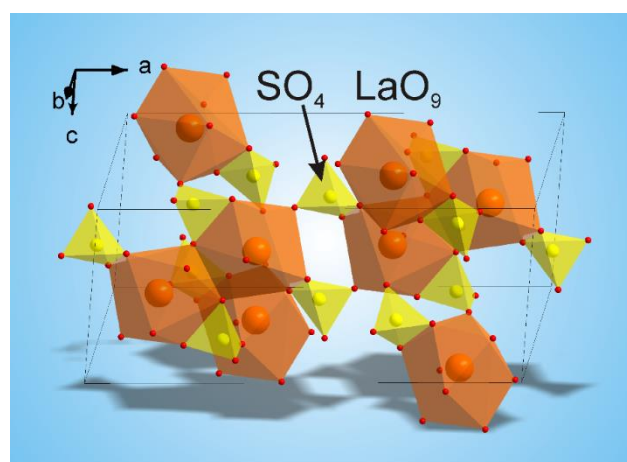
The unit cell parameters and the space group (C2/c) were determined using TOPAS 4.2 software [40]. It was found that parameters were close to the $\text{KTh}_2(\text{PO}_4)_3$ structure [41]; therefore, this crystal structure was selected as a starting model for Rietveld refinement. In particular, one site of Th^{4+} was occupied by the La^{3+} ion, the P^{5+} ion was replaced by the S^{6+} ion, and the K^+ site was removed. Such transformations led to the $\beta\text{-La}_2(\text{SO}_4)_3$ model, in which the thermal parameters of all ions were refined isotropically. The refinement was stable and yielded low R factors (Table 3 and Figure 3a). The coordinates of the atoms and main bond lengths are reported in Tables S1 and S2, respectively. The asymmetric part of the unit cell consisted of a single La^{3+} ion, which was coordinated by nine O^{2-} ions and two SO_4 tetrahedra (Figure 3b). In addition, the $[\text{LaO}_9]$ polyhedra were linked to each other by edges, forming two-dimensional layers in the bc plane. These 2D layers were bridged by $[\text{SO}_4]$ tetrahedra, forming a three-dimensional (3D) network (Figure 3b).

Table 3. Main parameters of $\beta\text{-La}_2(\text{SO}_4)_3$ processing and refinement.

Compound	$\beta\text{-La}_2(\text{SO}_4)_3$
Sp.Gr.	C2/c
$a, \text{\AA}$	17.6923 (9)
$b, \text{\AA}$	6.9102 (4)
$c, \text{\AA}$	8.3990 (5)
$\beta, ^\circ$	100.321 (3)
$V, \text{\AA}^3$	1010.22 (9)
Z	4
$2\theta\text{-interval}, ^\circ$	5–140
$R_{wp}, \%$	4.66
$R_p, \%$	3.67
$R_{exp}, \%$	1.46
χ^2	3.19
$R_B, \%$	1.36



(a)



(b)

Figure 3. (a) Different Rietveld plots of $\beta\text{-La}_2(\text{SO}_4)_3$ and (b) crystal structure of $\beta\text{-La}_2(\text{SO}_4)_3$.

According to the high-temperature X-ray diffraction data, the compound demonstrated positive anisotropic thermal expansion coefficients along all directions (Figure 4). However, along the a direction, in the temperature range of 300–450 K, the thermal expansion coefficient had an almost zero value. This behavior could be due to the stretching of zigzag chains consisting of LaO_9 polyhedra along the c direction, which, in the initial stages, could occur without a significant change in the layer thickness in the a direction

(Figure S2). In addition, we did not exclude the contribution of the deformation and filling of voids in the structure to the mechanism of this phenomenon.

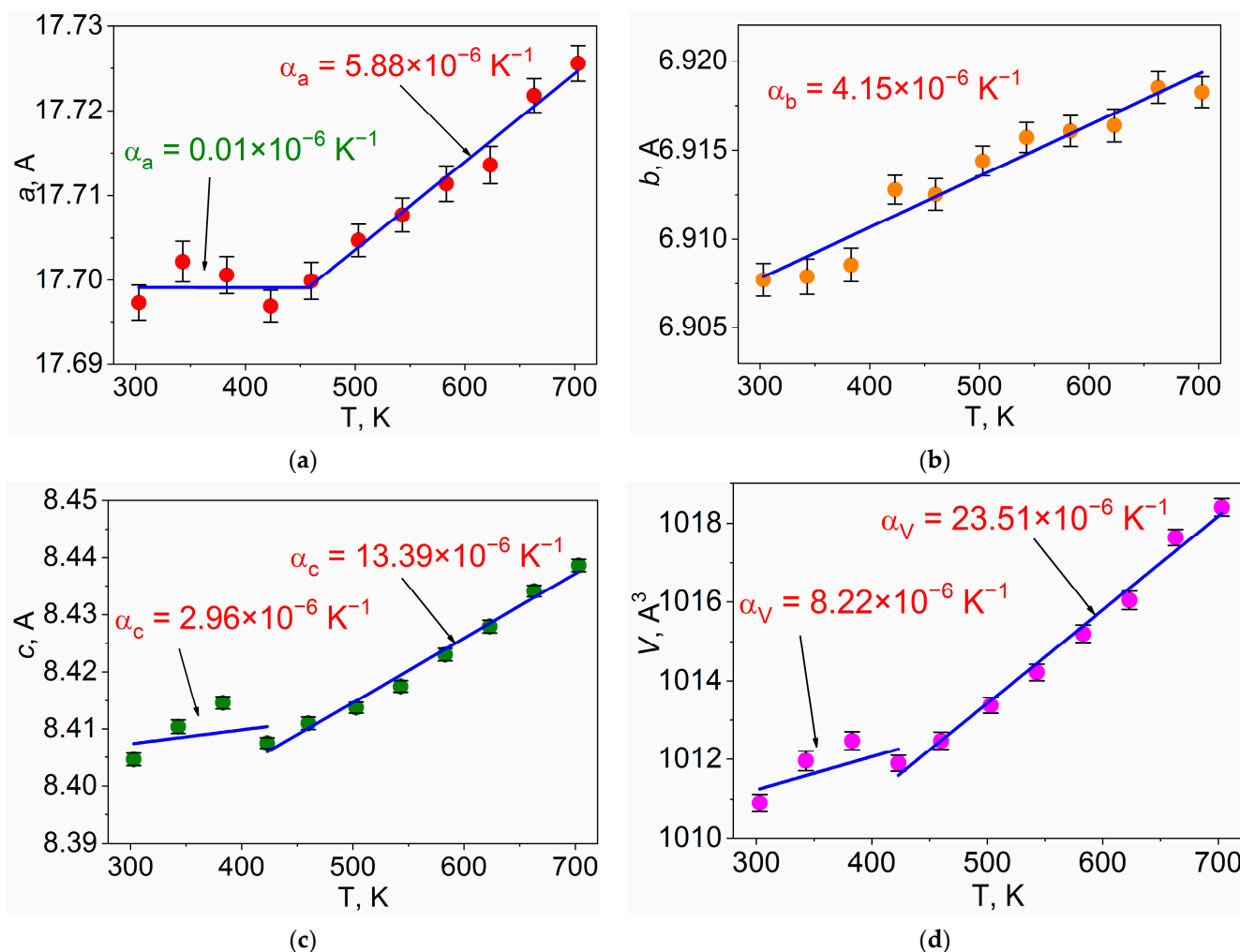


Figure 4. Thermal dependence of cell parameters *a* (a), *b* (b), *c* (c), and cell volume *V* (d) of β - $\text{La}_2(\text{SO}_4)_3$.

One additional interesting feature was the observation of discontinuity in the cell parameters and volume at 400 K (Figure 4). The XRD patterns did not reveal any new peaks or the disappearance of existing peaks, not any splitting of the main peak in the β - $\text{La}_2(\text{SO}_4)_3$ compound. This confirmed that the phase transition did not occur within the temperature range of 300–700 K, ensuring thermal stability. It is worth noting that nonlinear behavior of the cell parameters, transitioning from a linear to quadratic relationship, has been observed in various crystals [42–44]. For instance, a similar behavior was observed in single crystals of langasite and langatate upon heating from 300 to 700 K [3]. Another significant discovery was the consistent nonlinear increase in a specific heat of up to 700 K, beyond which the specific heat became independent of temperature due to a transition occurring above the Debye temperature (which was determined to be 740 K for these crystals). Considering this, it is reasonable to associate the change in trend of the cell parameters with the specific heat. In the case of this crystal, a temperature of 400 K may be in close proximity to its Debye temperature.

Upon investigation of the cell parameters in various chemical compositions, the findings revealed a notable increase in both *V* and *c* cell parameters, as Figure 5 illustrates. Intriguingly, despite the introduction of rare earth elements with larger ion radii, the *b* cell parameter remained constant. Moreover, the *a* cell parameter exhibited a visible downward

trend from the Pr element to the La element [34–36]. The β monoclinic angle experienced a significant variation in this direction as well. Presumably, this could be attributed to a declining pattern of one of the cell parameters combined with a nearly linear trend in cell volume over the entire range.

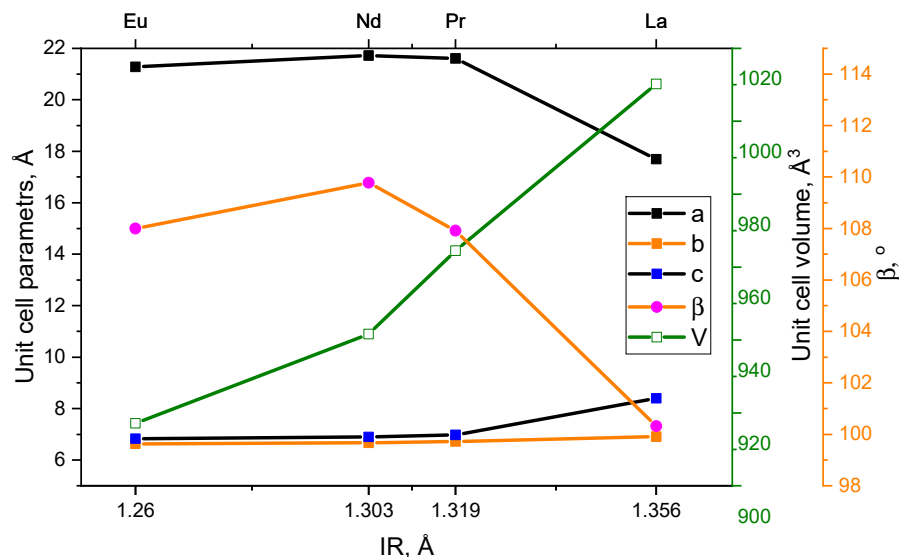


Figure 5. Evolution of structural parameters in sulfates of “light” rare earth elements.

2.3. Electronic Structure and Optical Properties

The Brillouin zone of β - $\text{La}_2(\text{SO}_4)_3$ and the electronic structure are shown in Figures 6a and 6b, respectively. A path through the high-symmetry points of the Brillouin zone was chosen as follows: Γ -C|C₂-Y₂- Γ -M₂-D|D₂-A- Γ |L₂- Γ -V₂. In addition, Figure 7a shows the subpaths with different colors. It is evident from Figure 7b that this compound performed as a dielectric material as the energy gap exceeded 6 eV. The bottom of the conduction band was located between the Γ and C points, and the top of the valence band was located at point Γ . Thus, applying the terminology for semiconductor materials [45], this compound was a material with an indirect band gap. However, the difference between indirect and direct (Γ - Γ) transition was very small and amounted to only 0.06 eV. Taking into account the well-known issue of underestimating band gaps if using LDA approximation, we performed a series of calculations using different approaches. In particular, the result of calculating the band gap value using the LDA model resulted in a value of 6.4 eV. The band gap values obtained using meta-GGA [46] and HSE06 [47] were 7.07 eV and 8.37 eV, respectively.

Figure 7a illustrates both the total electronic density of states (DOS) and the partial DOSes of β - $\text{La}_2(\text{SO}_4)_3$. According to the information depicted in Figure 7a, the top of the valence band was formed by the *p* electrons of the oxygen, while the bottom of the conduction band was predominantly determined by the *d* states of the La atom. In addition, the choice of calculation method (LDA, meta-GGA, or HSE06) did not affect the DOS configuration.

Figure 7b presents the experimental dependence of the Kubelka–Munk function for the β - $\text{La}_2(\text{SO}_4)_3$ compound (blue) compared with the Kubelka–Munk function for the β - $\text{RbEu}(\text{SO}_4)_2$ compound (black) [15] and with a theoretical LDA calculated from the absorption spectrum for lanthanum sulfate. The β - $\text{RbEu}(\text{SO}_4)_2$ Kubelka–Munk function presents the contribution of the charge transfer band of Eu^{3+} that is absent in β - $\text{La}_2(\text{SO}_4)_3$. As a result, function values for β - $\text{La}_2(\text{SO}_4)_3$ in the considered energy range below 6.4 eV were well below unity, in contrast with those for β - $\text{RbEu}(\text{SO}_4)_2$. This phenomenon was consistent with the LDA calculations, which indicated the presence of a fundamental absorption edge higher than 6.4 eV for the β - $\text{La}_2(\text{SO}_4)_3$ compound. An analysis of the electron localization (Figure S3) in the latter sulfate confirmed the nature of polarity of the

chemical bonds, which could be inferred by considering the electronegativity values. In particular, all S–O bonds and all La–O bonds in the sulfate could be considered covalent polar and ionic, respectively.

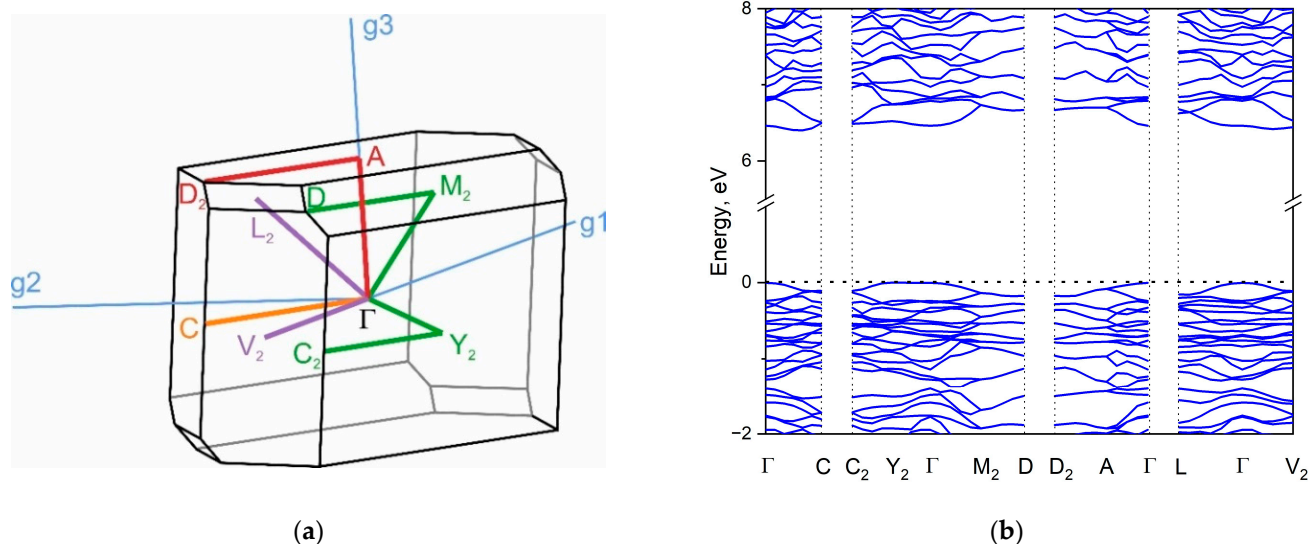


Figure 6. Brillouin zone (a) and electronic band structure (b) of $\beta\text{-La}_2(\text{SO}_4)_3$ calculated using local density approximation.

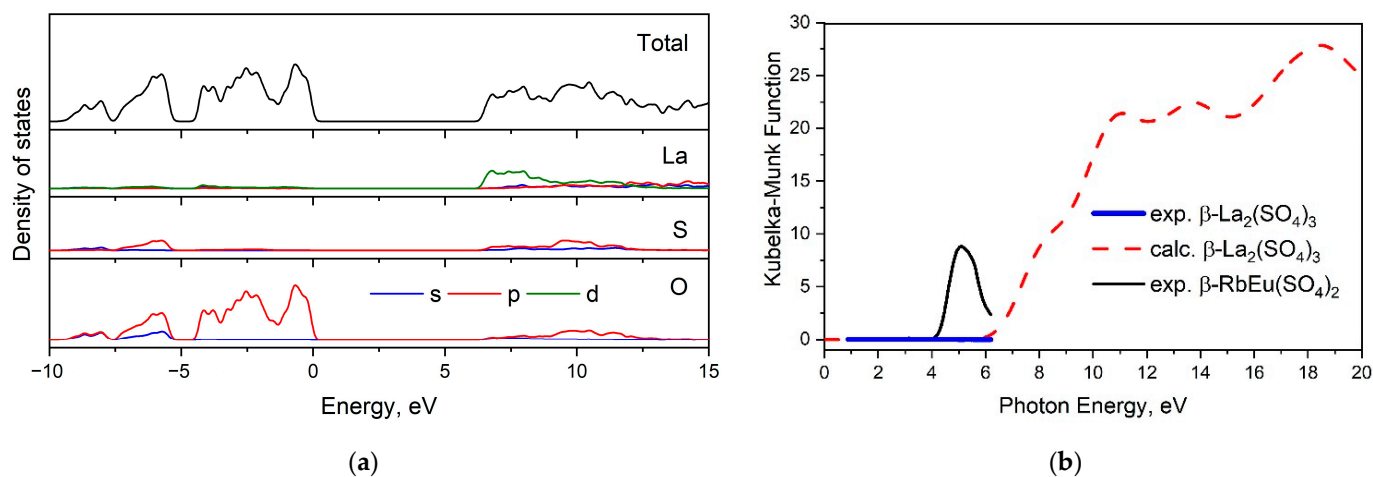


Figure 7. Total and partial density of electronic states (a), and comparison of the Kubelka–Munk function with results from the LDA-calculated absorption in $\beta\text{-La}_2(\text{SO}_4)_3$ (b).

Figure 8 presents the Raman and infrared spectra of $\beta\text{-La}_2(\text{SO}_4)_3$. Indeed, the experimental spectra were consistent with the calculated data, which indicated the coherence of the considered crystal parameters (Tables 3 and S2) with the sample structure. In both cases, the high wavenumber range (above 950 cm^{-1}) of the $\beta\text{-La}_2(\text{SO}_4)_3$ solid spectra corresponded to the stretching vibrations of the SO_4^{2-} ions [15]. A group of weakly intensive peaks from 375 to 700 cm^{-1} corresponded to the bending vibrations of the tetrahedral groups [34], while the lattice modes had a low intensity and were located below 300 cm^{-1} [48].

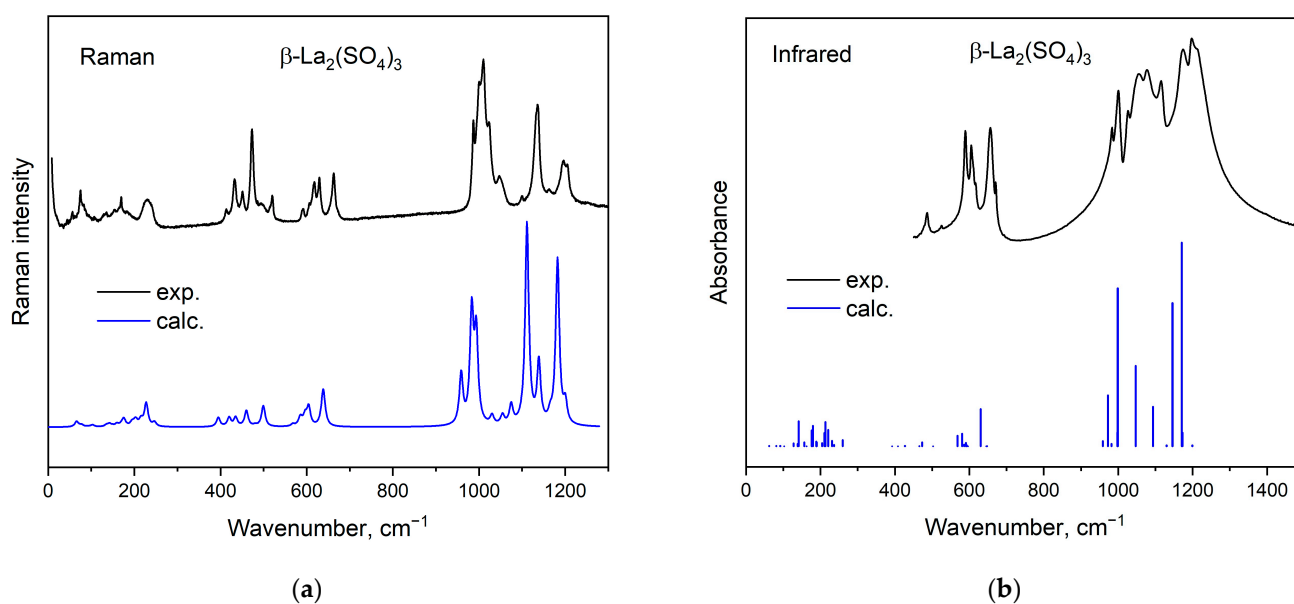


Figure 8. Comparison of the Raman (a) and infrared (b) spectra of $\beta\text{-La}_2(\text{SO}_4)_3$ with the results of the Raman profile and IR intensity simulation.

3. Methods and Materials

3.1. Synthesis

Anhydrous lanthanum sulfate was synthesized via high-temperature dehydration of the corresponding $\text{La}_2(\text{SO}_4)_3 \cdot 9\text{H}_2\text{O}$, which was obtained by recrystallization of a commercial reagent (Chemically pure, Novosibirsk Factory of Rare Metals, Novosibirsk, Russia). X-ray phase analysis confirmed the purity of the compound obtained after recrystallization (Figure S4 and Table S3) [49]. For the dehydration process, a weighed amount of the non-hydrate ($m = 5.00$ g) was placed in a corundum crucible and heated in a muffle furnace to a temperature of 500 °C in air. Afterward, it was left at this temperature for 24 h to yield a polycrystalline product, which was determined as anhydrous lanthanum sulfate according to the mass value ($m_{\text{exp}} = 3.96$ g, $m_{\text{theor}} = 3.98$ g).

3.2. Analysis Methods

The powder diffraction data of the $\beta\text{-La}_2(\text{SO}_4)_3$ substance for the Rietveld analysis was collected at room temperature using a Bruker D8 ADVANCE powder diffractometer ($\text{Cu-K}\alpha$ radiation) and linear VANTEC detector (Bruker AG, Germany). The step size of 2θ was 0.016° , and the counting time was 6 s per step. The 2θ range of $5\text{--}70^\circ$ was measured with a 0.6 mm divergence slit, but the 2θ range of $70\text{--}140^\circ$ was measured with a 2 mm divergence slit. Larger slits allowed for a noticeably increased intensity of high-angle peaks without a loss of resolution, because the high-angle peaks were broad enough to not be affected by the bigger divergence of the beam. The estimated standard deviation (ESD) $\sigma(I_i)$ of all points on patterns were calculated using intensities according to I_i : $\sigma(I_i) = I_i^{1/2}$. The intensities and obtained ESDs were further normalized, $I_{i\text{norm}} = I_i \times 0.6/(\text{slit width})$, $\sigma_{\text{norm}}(I_i) = \sigma(I_i) \times 0.6/(\text{slit width})$, taking into account an actual value of the divergence slit width, which was used to measure each particular intensity I_i . Thus, the transformed powder pattern had the usual view in the whole 2θ range $5\text{--}140^\circ$, but all high-angle points had small ESDs. An additional 11 XRD patterns were measured in the temperature range of $143\text{--}703$ K using Anton Paar heat attachments.

Thermal analysis in an argon flow was carried out using the Differential Thermal Analysis (DTA/TG) equipment 499 F5 Jupiter NETZSCH (Netzsch, GmbH & Co. KG, Hamburg, Germany). The powder samples were inserted into alumina crucibles. The heating rate was 3 °C/min. For enthalpy determination, the equipment was calibrated with the use of standard substances, such as In, Sn, Bi, Zn, Al, Ag, Au, and Ni. The heat

effect peaks were determined with the package “Proteus 6 2012”. The peak temperatures and areas in the parallel experiments were reproduced with an inaccuracy of less than 3%. Determination of the kinetic parameters was based on the Kissinger Equation (1) [50,51] in linearized form and on the Ozawa–Doyle Equation (2) [52,53]:

$$-\frac{1}{T} = \frac{1}{E} \cdot R \ln \frac{b}{T^2} - \frac{R}{E} \ln \frac{AR}{E} \quad (1)$$

$$\lg \beta + \frac{0.4567E}{RT} = C \quad (2)$$

where T is the temperature at the maximum reaction rate, b is the heating rate, E is the activation energy, A is the pre-exponential factor, R is the gas constant, and C is the constant.

Fourier-transform infrared spectroscopy (FTIR) measurements were carried out with the use of a Fourier-Transform Infrared Spectrometer FSM 1201 (Infraspek Ltd., St. Petersburg, Russia). The sample for investigation was prepared in tablet form with the addition of annealed KBr. Raman spectra at an ambient condition in the spectral range of 10–1500 cm^{-1} were recorded using a Horiba Jobin Yvon T64000 (Horiba, Lille, France) spectrometer equipped with a triple monochromator in subtractive mode. The spectral resolution was 2 cm^{-1} (this resolution was achieved using 1800 str/mm gratings and 100 μm slits) with a dot density of 3 pixel/ cm^{-1} . The spectra were excited using a diode-pumped solid-state single-mode laser Spectra-Physics Excelsior-532-300-CDRH (USA) with a wavelength of 532 nm and power of <1 mW. Scattered radiation was collected via a microscope based on Olympus BX-41 (Olympus, Tokyo, Japan) through the objective Olympus MPlan50x (Olympus, Japan) with a numerical aperture of N.A. = 0.75. The diffuse reflectance spectra were measured on a UV-2600 spectrophotometer (Shimadzu, Tokyo, Japan) equipped with an ISR-2600 Plus attachment with an integrating sphere. The optical band gap was estimated based on the diffuse reflectance spectra measurements.

3.3. Calculation Methods

First-principle calculations in this study utilized the density functional theory (DFT) approach, implemented in CASTEP code [54]. The $5d^1 6s^2$, $3s^2 3p^4$, and $2s^2 2p^4$ valence electron configurations were considered for La, S, and O atoms, respectively. To perform the calculations, the local density approximation (LDA) method was employed, based on the Perdew and Zunger parametrization [55] of the numerical results by Ceperley and Alder [56]. Norm-conserving pseudopotentials were used, with a cutoff energy for the plane basis set at 1030 eV. During geometry optimization, a tolerance level of 1.0×10^{-3} eV/Å was chosen for maximal forces and 0.01 GPa was chosen for maximal stresses. The Monkhorst-Pack k-point integration network of the Brillouin zone was chosen as $3 \times 3 \times 3$. Density functional perturbation theory [57,58] was employed to calculate the phonon spectra at the center of the Brillouin zone and to determine the Raman tensor components (spectral profile) and infrared intensities.

4. Conclusions

In this study, our investigation of anhydrous lanthanum sulfate resulted in the discovery of a new polymorphic modification. This finding contributes to the ever-expanding range of structural types within the sulfates of rare earth elements. Furthermore, our investigation revealed a noteworthy trend: as the chemical composition is simplified, the enthalpy values of the thermochemical processes tend to decrease. This insight can provide valuable information regarding energy changes that occur during thermochemical process. Moreover, we investigated the decomposition reactions of $\text{Ln}_2(\text{SO}_4)_3$ and $\text{Ln}_2\text{O}_2\text{SO}_4$ sulfates, focusing specifically on the ionic radius of lanthanides. By understanding the influence of the ionic radii, it may be possible to predict and design the properties of compounds for future applications. The $\beta\text{-La}_2(\text{SO}_4)_3$ compound was found to be a dielectric material with a bandgap larger than 6.4 eV. The valence band was found to be primarily composed

of *p*-electrons of oxygen, while the conduction band was predominantly determined by the *d* states of La. The experimental Raman and infrared spectra were consistent with the calculated data, confirming the accuracy of the obtained parameters of the crystal structure. The results reported here could contribute to the broader field of sulfates of rare earth elements and pave the path for further studies in this area. To summarize, this manuscript offers valuable insights into the crystal structure, thermochemistry, and optical properties of anhydrous lanthanum sulfate.

Supplementary Materials: The following supporting information can be downloaded at: <https://www.mdpi.com/article/10.3390/inorganics11110434/s1>, Figure S1: Heat effect showing up in dependence of heating rate for processes of destruction of lanthanum sulfates; Figure S2: Chain structure of LaO₉ polyhedra (a) and proposed mechanism of zero thermal expansion in the β-La₂(SO₄)₃ structure (b); Figure S3: Electron localization function in β-La₂(SO₄)₃ calculated using local density approximation; Figure S4: Difference Rietveld plot of the La₂(SO₄)₃·9H₂O compound; Table S1: Fractional atomic coordinates and isotropic displacement parameters (Å²) of β-La₂(SO₄)₃; Table S2: Main bond lengths (Å) of β-La₂(SO₄)₃; Table S3: Main parameters of processing and refinement of the La₂(SO₄)₃·9H₂O sample; Supplementary details concerning the crystal structure may be obtained from Fachinformationszentrum Karlsruhe, 76,344 Eggenstein-Leopoldshafen, Germany (fax: (+49)7247-808-666; e-mail: crystdata@fiz-karlsruhe.de; http://www.fiz-karlsruhe.de/request_for_deposited_data.html (accessed on 8 October 2023) on quoting the deposition number CSD-2298422.

Author Contributions: Conceptualization, Y.G.D. and K.M.-B.; methodology, S.A.B., M.S.M., A.S.O., M.A.Z., N.A.K. and A.S.A.; software, M.S.M., A.S.O. and M.A.Z.; validation, S.A.B. and Y.G.D.; investigation, S.A.B., M.S.M., A.S.K., E.I.S. and N.O.A.; resources, M.S.M., N.A.S. and K.M.-B.; data curation, Y.G.D.; writing—original draft preparation, S.A.B., M.S.M., A.S.O., M.A.Z., N.A.K., K.M.-B. and Y.G.D.; writing—review and editing, S.A.B., M.S.M., K.M.-B. and Y.G.D.; visualization, S.A.B., M.S.M., A.S.O. and N.O.A.; supervision, Y.G.D.; project administration, N.A.S., K.M.-B. and Y.G.D. All authors have read and agreed to the published version of the manuscript.

Funding: The work was partly carried out within the framework of the Strategic Academic Leadership Program “Priority-2030” for the Kazan Federal University and the state assignment of the Kirensky Institute of Physics.

Data Availability Statement: The data that support the findings of this study are available from the corresponding author upon reasonable request.

Acknowledgments: We acknowledge Lisa-Marie Wagner (JLU Giessen) for help with X-ray powder diffractometry, and Svetlana Volkova and Irina Palamarchuk (UTMN) for help with IR- and UV-spectrometry. The use of equipment provided by the Krasnoyarsk Regional Center of Research Equipment of Federal Research Center “Krasnoyarsk Science Center SB RAS” is acknowledged.

Conflicts of Interest: The authors declare no conflict of interest.

References

1. Han, K.N. Characteristics of precipitation of rare earth elements with various precipitants. *Minerals* **2020**, *10*, 178. [[CrossRef](#)]
2. Amato, A.; Becci, A.; Birloaga, I.; De Michelis, I.; Ferella, F.; Innocenzi, V.; Ippolito, N.M.; Gomez, C.P.J.; Vegliò, F.; Beolchini, F. Sustainability analysis of innovative technologies for the rare earth elements recovery. *Renew. Sustain. Energy Rev.* **2019**, *106*, 41–53. [[CrossRef](#)]
3. Binnemans, K.; Jones, P.T.; Blanpain, B.; Gerven, T.V.; Yang, Y.; Walton, A.; Buchert, M. Recycling of rare earths: A critical review. *J. Clean. Prod.* **2013**, *51*, 1–22. [[CrossRef](#)]
4. Xie, F.; Zhang, T.A.; Dreisinger, D.; Doyle, F. A critical review on solvent extraction of rare earths from aqueous solutions. *Miner. Eng.* **2014**, *56*, 10–28. [[CrossRef](#)]
5. Bao, W.; Liu, D.; Li, P.; Duan, Y. Structural properties, elastic anisotropies and thermal conductivities of tetragonal LnB₂C₂ (Ln = Rare Earth) compounds from first-principles calculations. *Ceram. Int.* **2019**, *45*, 1857–1867. [[CrossRef](#)]
6. Guo, D.; Moreno-Ramírez, L.M.; Law, J.-Y.; Zhang, Y.; Franco, V. Excellent cryogenic magnetocaloric properties in heavy rare-earth based HRENiGa₂ (HRE = Dy, Ho, or Er) compounds. *Sci. China Mater.* **2023**, *66*, 249–256. [[CrossRef](#)]
7. Gupta, P.; Mahapatra, P.K.; Choudhary, R.N.P. Structural and electrical characteristics of rare-earth modified bismuth layer structured compounds. *J. Alloys Compd.* **2021**, *863*, 158457. [[CrossRef](#)]
8. Zhang, R.; Wang, Z.; Xu, X.; Mao, X.; Xiong, J.; Yang, Y.; Han, K. All-inorganic rare-earth halide double perovskite single crystals with highly efficient photoluminescence. *Adv. Opt. Mater.* **2021**, *9*, 2100689. [[CrossRef](#)]

9. Batchu, N.K.; Li, Z.; Verbelen, B.; Binnemans, K. Structural effects of neutral organophosphorus extractants on solvent extraction of rare-earth elements from aqueous and non-aqueous nitrate solutions. *Sep. Purif. Technol.* **2021**, *255*, 117711. [[CrossRef](#)]
10. Silva, R.G.; Morais, C.A.; Teixeira, L.V.; Oliveira, É.D. Selective precipitation of high-quality rare earth oxalates or carbonates from a purified sulfuric liquor containing soluble impurities. *Min. Metall. Explor.* **2019**, *36*, 967–977. [[CrossRef](#)]
11. Geneyton, A.; Foucaud, Y.; Filippov, L.O.; Menad, N.-E.; Renard, A.; Badawi, M. Synergistic adsorption of lanthanum ions and fatty acids for efficient rare-earth phosphate recovery: Surface analysis and ab initio molecular dynamics studies. *Appl. Surf. Sci.* **2020**, *526*, 146725. [[CrossRef](#)]
12. Zhou, Y.; Liu, J.; Cheng, G.; Xue, X.; Yang, H. Kinetics and mechanism of hydrochloric acid leaching of rare earths from Bayan Obo slag and recovery of rare earth oxalate and high purity oxides. *Hydrometallurgy* **2022**, *208*, 105782. [[CrossRef](#)]
13. Huang, W.; Chen, W.; Bai, Q.; Zhang, Z.; Feng, M.; Zheng, Z. Anion-guided stepwise assembly of high-nuclearity lanthanide hydroxide clusters. *Angew. Chem.* **2022**, *134*, e202205385. [[CrossRef](#)]
14. Jiao, D.-X.; Zhang, H.-L.; Li, X.-F.; He, C.; Li, J.-H.; Wei, Q.; Yang, G.-Y. YSO₄F·H₂O: A Deep-Ultraviolet Birefringent Rare-Earth Sulfate Fluoride with Enhanced Birefringence Induced by Fluorinated Y-Centered Polyhedra. *Inorg. Chem.* **2023**, *62*, 17333–17340. [[CrossRef](#)] [[PubMed](#)]
15. Denisenko, Y.G.; Molokeev, M.S.; Jiang, X.; Sedykh, A.E.; Aleksandrovsky, A.S.; Oreshonkov, A.S.; Roginskii, E.M.; Zhernakov, M.A.; Heuler, D.; Souffert, M.; et al. Negative thermal expansion in the polymorphic modification of double sulfate β-AEu(SO₄)₂ (A=Rb⁺, Cs⁺). *Inorg. Chem.* **2023**, *62*, 12423–12433. [[CrossRef](#)] [[PubMed](#)]
16. Denisenko, Y.G.; Khritokhin, N.A.; Andreev, O.V.; Basova, S.A.; Sal'nikova, E.I.; Polkovnikov, A.A. Thermal decomposition of europium sulfates Eu₂(SO₄)₃·8H₂O and EuSO₄. *J. Solid State Chem.* **2017**, *255*, 219–224. [[CrossRef](#)]
17. Buyer, C.; Enseling, D.; Jüstel, T.; Schleid, T. Hydrothermal synthesis, crystal structure, and spectroscopic properties of pure and Eu³⁺-doped NaY[SO₄]₂·H₂O and its anhydrate NaY[SO₄]₂. *Crystals* **2021**, *11*, 575. [[CrossRef](#)]
18. Pasechnik, L.A.; Peshonova, A.O.; Lipina, O.A.; Medyankina, I.S.; Enyashin, A.N.; Chufarov, A.Y.; Tyutyunnik, A.P. Co-crystallization of red emitting (NH₄)₃Sc(SO₄)₃:Eu³⁺ microfibers: Structure–luminescence relationship for promising application in optical thermometry. *CrystEngComm* **2022**, *24*, 4819–4830. [[CrossRef](#)]
19. Pasechnik, L.A.; Medyankina, I.S.; Yatsenko, S.P. Scandium extraction from multicomponent systems by crystallization of complex sulfates. *IOP Conf. Ser. Mater. Sci. Eng.* **2020**, *848*, 012064. [[CrossRef](#)]
20. Thomsen, M.S.; Sørensen, T.J. Delicate, a study of the structural changes in ten-coordinated La (III), Ce (III), Pr (III), Nd (III), Sm (III) and Eu (III) sulfates. *Dalton Trans.* **2022**, *51*, 8964–8974. [[CrossRef](#)]
21. Haghghat, M.; Narioie, A.; Rezvani, A.; Hakimi, M.; Saravani, H.; Darroudi, M.; Amini, A.; Sabaghan, M.; Khatami, M. Anticancer property of lanthanide sulfate nanostructure against neuroblastoma-neuro2a cell line. *BioNanoScience* **2021**, *11*, 696–702. [[CrossRef](#)]
22. Das, G.; Lencka, M.M.; Eslamianesh, A.; Wang, P.; Anderko, A.; Riman, R.E.; Navrotsky, A. Rare earth sulfates in aqueous systems: Thermodynamic modeling of binary and multicomponent systems over wide concentration and temperature ranges. *J. Chem. Thermodyn.* **2019**, *131*, 49–79. [[CrossRef](#)]
23. Niinistö, L.; Leskelä, M. Inorganic complex compounds II. *Handb. Phys. Chem. Rare Earths* **1987**, *9*, 91–320.
24. Denisenko, Y.G.; Sedykh, A.E.; Basova, S.A.; Atuchin, V.V.; Molokeev, M.S.; Aleksandrovsky, A.S.; Krylov, A.S.; Oreshonkov, A.S.; Khritokhin, N.A.; Sal'nikova, E.I.; et al. Exploration of the structural, spectroscopic and thermal properties of double sulfate monohydrate NaSm(SO₄)₂·H₂O and its thermal decomposition product NaSm(SO₄)₂. *Adv. Powder Technol.* **2021**, *32*, 3943–3953. [[CrossRef](#)]
25. Tunsu, C.; Petranikova, M.; Gergoric, M.; Ekberg, C.; Retegan, T. Reclaiming rare earth elements from end-of-life products: A review of the perspectives for urban mining using hydrometallurgical uni toperations. *Hydrometallurgy* **2015**, *156*, 239–258. [[CrossRef](#)]
26. Zhu, Z.; Pranolo, Y.; Cheng, C.Y.; Cheng, C.Y. Separation of uranium and thorium from rare earths for rare earth production—A review. *Miner. Eng.* **2015**, *77*, 185–196. [[CrossRef](#)]
27. Beltrami, D.; Deblonde, G.-P.; Bélaïr, S.; Weigel, V.; Bélaïr, S.; Weigel, V. Recovery of yttrium and lanthanides from sulfate solutions with high concentration of iron and low rare earth content. *Hydrometallurgy* **2015**, *157*, 356–362. [[CrossRef](#)]
28. Diaz, L.A.; Lister, T.E.; Parkman, J.A.; Clark, G.G. Comprehensive process for the recovery of value and critical materials from electronic waste. *J. Clean. Prod.* **2016**, *125*, 236–244. [[CrossRef](#)]
29. Kelley, S.P.; Nuss, J.S.; Rogers, R.D. Using crystal structures of ionic compounds to explore complexation and extraction of rare earth elements in ionic liquids. In *Application of Ionic Liquids on Rare Earth Green Separation and Utilization*; Springer: Berlin/Heidelberg, Germany, 2015; pp. 21–42.
30. Zhao, Z.; Qiu, Z.; Yang, J.; Lu, S.; Cao, L.; Zhang, W.; Xu, Y. Recovery of rare earth elements from spent fluid catalytic cracking catalysts using leaching and solvent extraction techniques. *Hydrometallurgy* **2017**, *167*, 183–188. [[CrossRef](#)]
31. Hatada, N.; Shizume, K.; Uda, T. Discovery of rapid and reversible water insertion in rare earth sulfates: A new process for thermochemical heat storage. *Adv. Mater.* **2017**, *29*, 1606569. [[CrossRef](#)]
32. Wickleder, M.S. Inorganic lanthanide compounds with complex anions. *Chem. Rev.* **2002**, *102*, 2011–2088. [[CrossRef](#)]
33. Choi, M.-H.; Kim, M.K.; Jo, V.; Lee, D.W.; Shim, I.-W.; Ok, K.M. Hydrothermal syntheses, structures, and characterizations of two lanthanide sulfate hydrates materials, La₂(SO₄)₃·H₂O and Eu₂(SO₄)₃·4H₂O. *Bull. Korean Chem. Soc.* **2010**, *31*, 1077–1080. [[CrossRef](#)]

34. Denisenko, Y.G.; Atuchin, V.V.; Molokeev, M.S.; Sedykh, A.E.; Khritokhin, N.A.; Aleksandrovsky, A.S.; Oreshonkov, A.S.; Shestakov, N.P.; Adichtchev, S.V.; Pugachev, A.M.; et al. Exploration of the crystal structure and thermal and spectroscopic properties of monoclinic praseodymium sulfate $\text{Pr}_2(\text{SO}_4)_3$. *Molecules* **2022**, *27*, 3966. [[CrossRef](#)] [[PubMed](#)]
35. Sirotinkin, S.P.; Efremov, V.A.; Kovba, L.M.; Pokrovsky, A.N. Crystal structure of anhydrous neodymium sulfate $\text{Nd}_2(\text{SO}_4)_3$. *Kristallografiya* **1977**, *22*, 1272–1273.
36. Denisenko, Y.G.; Aleksandrovsky, A.S.; Atuchin, V.V.; Krylov, A.S.; Molokeev, M.S.; Oreshonkov, A.S.; Shestakov, N.P.; Andreev, O.V. Exploration of structural, thermal and spectroscopic properties of self-activated sulfate $\text{Eu}_2(\text{SO}_4)_3$ with isolated SO_4 groups. *J. Ind. Eng. Chem.* **2018**, *68*, 109–116. [[CrossRef](#)]
37. Lobanov, N.N.; Kuznetsova, T.A. Crystal chemistry of lanthanide oxochlorotungstates. *Russ. J. Inorg. Chem.* **2008**, *53*, 1256–1262. [[CrossRef](#)]
38. Dzhurinskii, B.F. Periodicity of properties of rare earth elements. *Russ. J. Inorg. Chem.* **1980**, *25*, 79–86. (In Russian)
39. Wickleder, M.S. $\text{La}(\text{NH}_2\text{SO}_3)_3$: Einkristalle eines wasserfreien Amidosulfates der Selten-Erd-Elemente durch schonende Entwässerung von $\text{La}(\text{NH}_2\text{SO}_3)_3 \cdot 2.5\text{H}_2\text{O}$. *Z. Anorg. Allg. Chem.* **1999**, *625*, 1794–1798. [[CrossRef](#)]
40. Topas, B.A. V4: General profile and structure analysis software for powder diffraction data. In *User's Manual*; Bruker AXS: Karlsruhe, Germany, 2008.
41. Matkovic, B.; Prodic, B.; Slijkic, M. Crystal structure of potassium dithorium triphosphate $\text{KTh}_2(\text{PO}_4)_3$. *Croat. Chem. Acta* **1968**, *40*, 147–161.
42. Kräußlich, J.; Höfer, S.; Zastrau, U.; Jeutter, N.; Baehz, C. Temperature dependence of lattice parameters of langasite single crystals. *Cryst. Res. Technol.* **2010**, *45*, 490–492. [[CrossRef](#)]
43. Liu, Y.; Jiang, X.; Molokeev, M.S.; Zhang, X.; Lin, Z. $\text{Zn}_3\text{GaB}_6\text{O}_{12}\text{As}$ and $\text{Zn}_4\text{P}_6\text{N}_{12}\text{S}$: Isotropic Zero Thermal Expansion Materials Based on the “Cage-Restricting” Model. *Chem. Mater.* **2022**, *34*, 9915–9922. [[CrossRef](#)]
44. Kugaenko, O.M.; Uvarova, S.S.; Krylov, S.A.; Senatulin, B.R.; Petrakov, V.S.; Buzanov, O.A.; Egorov, V.N.; Sakharov, S.A. Basic thermophysical parameters of langasite ($\text{La}_3\text{Ga}_5\text{SiO}_{14}$), langatate ($\text{La}_3\text{Ta}_{0.5}\text{Ga}_{5.5}\text{O}_{14}$), and catangasite ($\text{Ca}_3\text{TaGa}_3\text{Si}_2\text{O}_{14}$) single crystals in a temperature range of 25 to 1000 °C. *Bull. Russ. Acad. Sci. Phys.* **2012**, *76*, 1258–1263. [[CrossRef](#)]
45. Yuan, L.-D.; Deng, H.-X.; Li, S.-S.; Wei, S.-H.; Luo, J.-W. Unified theory of direct or indirect band-gap nature of conventional semiconductors. *Phys. Rev. B* **2018**, *98*, 245203. [[CrossRef](#)]
46. Bartók, A.P.; Yates, J.R. Regularized SCAN Functional. *J. Chem. Phys.* **2019**, *150*, 161101. [[CrossRef](#)] [[PubMed](#)]
47. Krukau, A.V.; Vydrov, O.A.; Izmaylov, A.F.; Scuseria, G.E. Influence of the Exchange Screening Parameter on the Performance of Screened Hybrid Functionals. *J. Chem. Phys.* **2006**, *125*, 224106. [[CrossRef](#)] [[PubMed](#)]
48. BChoi, K.; Lockwood, D.J. Raman spectrum of Na_2SO_4 (phase V). *Solid State Commun.* **1989**, *72*, 133–137.
49. Sherry, E.G. The structure of $\text{Pr}_2(\text{SO}_4)_3(\text{H}_2\text{O})_8$ and $\text{La}_2(\text{SO}_4)_3(\text{H}_2\text{O})_9$. *J. Solid State Chem.* **1976**, *19*, 271–279. [[CrossRef](#)]
50. Blaine, R.L.; Kissinger, H.E. Homer Kissinger and the Kissinger equation. *Thermochim. Acta* **2012**, *540*, 1–6. [[CrossRef](#)]
51. Llopiz, J.; Romero, M.M.; Jerez, A.; Laureiro, Y. Generalization of the Kissinger equation for several kinetic models. *Thermochim. Acta* **1995**, *256*, 205–211. [[CrossRef](#)]
52. Ozawa, T. A new method of analyzing thermogravimetric data. *Bull. Chem. Soc. Jpn.* **1965**, *38*, 1881–1886. [[CrossRef](#)]
53. Doyle, C.D. Kinetic analysis of thermogravimetric data. *J. Appl. Polym. Sci.* **1961**, *15*, 285–292. [[CrossRef](#)]
54. Clark, S.J.; Segall, M.D.; Pickard, C.J.; Hasnip, P.J.; Probert, M.I.J.; Refson, K.; Payne, M.C. First Principles Methods Using CASTEP. *Z. Für Krist. Cryst. Mater.* **2005**, *220*, 567–570. [[CrossRef](#)]
55. Perdew, J.P.; Zunger, A. Self-Interaction Correction to Density-Functional Approximations for Many-Electron Systems. *Phys. Rev. B* **1981**, *23*, 5048–5079. [[CrossRef](#)]
56. Ceperley, D.M.; Alder, B.J. Ground State of the Electron Gas by a Stochastic Method. *Phys. Rev. Lett.* **1980**, *45*, 566–569. [[CrossRef](#)]
57. Refson, K.; Tulip, P.R.; Clark, S.J. Variational Density-Functional Perturbation Theory for Dielectrics and Lattice Dynamics. *Phys. Rev. B* **2006**, *73*, 155114. [[CrossRef](#)]
58. Porezag, D.; Pederson, M.R. Infrared Intensities and Raman-Scattering Activities within Density-Functional Theory. *Phys. Rev. B* **1996**, *54*, 7830–7836. [[CrossRef](#)]

Disclaimer/Publisher's Note: The statements, opinions and data contained in all publications are solely those of the individual author(s) and contributor(s) and not of MDPI and/or the editor(s). MDPI and/or the editor(s) disclaim responsibility for any injury to people or property resulting from any ideas, methods, instructions or products referred to in the content.